

Cite this: *RSC Adv.*, 2019, 9, 8065

Ag₃PO₄ nanocrystals and g-C₃N₄ quantum dots decorated Ag₂WO₄ nanorods: ternary nanoheterostructures for photocatalytic degradation of organic contaminants in water†

Chang Liu,^a Jingbo Wang,^b Shuang Yang,^b Xiuying Li^{*a} and Xue Lin^{†b}

Visible-light-driven Ag₃PO₄/graphite-like carbon nitride/Ag₂WO₄ photocatalysts with different weight fractions of Ag₃PO₄ were synthesized. Ag₂WO₄ nanorods with a scale of 500 nm to 3 μm were prepared by using a hydrothermal reaction. Via a facile deposition–precipitation technique, graphite-like carbon nitride (g-C₃N₄) quantum dots and Ag₃PO₄ nanocrystals were then deposited onto the surface of Ag₂WO₄ nanorods sequentially. Under visible-light irradiation (λ > 420 nm), the Ag₃PO₄/g-C₃N₄/Ag₂WO₄ nanorods degraded Rh B efficiently and displayed much higher photocatalytic activity than that of pure Ag₂WO₄ and the g-C₃N₄/Ag₂WO₄ composite, and the Ag₃PO₄/g-C₃N₄/Ag₂WO₄ hybrid photocatalyst with 30 wt% of Ag₃PO₄ exhibited the highest photocatalytic activity. The quenching effects of different scavengers demonstrated that reactive h⁺ and ·O²⁻ played the major roles in Rh B degradation. It was elucidated that the excellent photocatalytic activity of Ag₃PO₄/g-C₃N₄/Ag₂WO₄ for the degradation of Rh B under visible light (λ > 420 nm) can be ascribed to the efficient separation of photogenerated electrons and holes through the Ag₃PO₄/g-C₃N₄/Ag₂WO₄ heterostructure.

Received 29th November 2018
Accepted 27th February 2019

DOI: 10.1039/c8ra09815h

rsc.li/rsc-advances

1. Introduction

The development of visible-light-driven photocatalysts with excellent performance and good stability is a precondition for harvesting more sunlight and realizing efficient photocatalysis. In recent years, Ag-based photocatalysts, such as AgX (where X = Cl, Br, and I), Ag₂O, Ag₂CO₃, Ag₆Si₂O₇, Ag₂WO₄, Ag₃PO₄, and Ag₂Mo₂O₇, have been developed for photocatalysis applications.^{1–8} Among those Ag-based photocatalysts, Ag₂WO₄ has been the most studied because of its weak crystal field and was verified to exhibit H₂ evolution and organic pollution degradation ability under UV light irradiation.⁹ However, the band gap of Ag₂WO₄ is theoretically calculated to be 3.55 eV, resulting in its sluggish reaction to visible light, like TiO₂.¹⁰ Thereupon, many efforts have been devoted to make Ag₂WO₄ sensitive to visible light, including its combination with sensitizers, *i.e.*, AgI, Ag/AgCl, and Ag. Unfortunately, Ag₂WO₄ itself has not yet been modified to be sensitive to visible light.^{11–13} However, some researchers found that Ag₃PO₄ shows strong oxidation power, which can achieve quantum efficiency of up to 90% under visible light for O₂ generation from water splitting.^{14,15} However,

as Ag₃PO₄ is light-sensitive and slightly soluble in aqueous solution, it will be photocorroded and decompose to weakly active Ag during the photodegradation, and, accordingly, the photocatalytic activity gradually deteriorates, which is the main hindrance for the practical application of Ag₃PO₄ as a recyclable and highly efficient photocatalyst. Recent reports have shown that forming complexes with special structures such as core-shell nanostructures, plasmonic structures, and heterostructures could not only effectively protect the Ag₃PO₄ crystals from dissolution in aqueous solutions but also enhance their stabilities and photocatalytic performance.^{15,16} Therefore, modifying Ag₂WO₄ with Ag₃PO₄ could significantly accelerate the transfer of photogenerated charge carriers.

Nowadays, graphite-like carbon nitride (g-C₃N₄) has been studied as a promising candidate for hydrogen evolution and environment purification under visible-light irradiation.^{17–19} Although g-C₃N₄ possesses good chemical and thermal stability, its use in photocatalysis is limited because of its high recombination of photogenerated electron–hole pairs.²⁰ To solve this problem, abundant strategies, including doping, deposition, and sensitization, were developed.^{20–23} Constructing the heterostructure is also an effective approach for decreasing the recombination rate of photogenerated charges. However, most of the reported g-C₃N₄ nanostructures are composed of stacked two-dimensional nanosheets, and very few available examples concentrating on zero-dimensional quantum dots (QDs) exist, especially on QD-based heterostructures.^{19,24} Given the

^aKey Laboratory of Preparation and Application of Environmental Friendly Materials, Jilin Normal University, Ministry of Education, Changchun 130103, China

^bCollege of Material Science and Engineering, Beihua University, Jilin 132013, China. E-mail: jlsdlinxue@126.com; Fax: +86 434 329 2154; Tel: +86 1569434 9717

† Electronic supplementary information (ESI) available. See DOI: 10.1039/c8ra09815h

enhanced light absorption and, more importantly, excellent electron conductivity of carbon materials, it is rationally speculated that decoration of Ag_2WO_4 with $\text{g-C}_3\text{N}_4$ QDs in an intimate integration fashion would significantly improve the photocatalytic performances of Ag_2WO_4 .

Herein, we report a successful attempt at the preparation of $\text{Ag}_3\text{PO}_4/\text{g-C}_3\text{N}_4/\text{Ag}_2\text{WO}_4$ nanoheterostructures via a facile *in situ* precipitation synthetic strategy. The photocatalytic performance of the ternary composite was investigated by measuring the photodegradation of rhodamine B (Rh B) under visible-light irradiation ($\lambda > 420$ nm). Up to date, construction of $\text{Ag}_3\text{PO}_4/\text{g-C}_3\text{N}_4/\text{Ag}_2\text{WO}_4$ ternary heterostructures in combination with a systematic study on the photocatalysis mechanism has not yet been reported.

2. Experimental

2.1 Preparation of photocatalysts

2.1.1 Preparation of Ag_2WO_4 nanorods. All reagents for synthesis and analysis were commercially available and used without further treatments. The Ag_2WO_4 nanorods were synthesized through a facile hydrothermal method. In a typical procedure, a solution of Na_2WO_4 (0.10 mol L^{-1} , $10 \text{ mL H}_2\text{O}$) was stirred for 30 min, then 20 mL aqueous solution of AgNO_3 (0.40 mol L^{-1} , $5 \text{ mL H}_2\text{O}$) was dropped slowly into the above solution, which was stirred magnetically for another 30 min. The mixed solution was transferred into a 20 mL Teflon-lined steel autoclave, which was heated in an oven at 160°C for 24 h. Then the system was allowed to cool to room temperature naturally. Lastly, the obtained samples were collected and washed with ethanol and distilled water several times then and dried at 70°C for 2 h.

2.1.2 Preparation of $\text{g-C}_3\text{N}_4$ QDs. Bulk $\text{g-C}_3\text{N}_4$ was prepared by heating melamine for 4 h to 550°C and keeping it at this temperature for another 4 h in air.²⁴ $\text{g-C}_3\text{N}_4$ QDs was prepared by using Yu's method:²⁴ First, 1 g of bulk $\text{g-C}_3\text{N}_4$ was treated in the mixture of concentrated sulfuric acid (H_2SO_4) (20 mL) and nitric acid (HNO_3) (20 mL) for $\sim 2 \text{ h}$ at room temperature. The mixture was then diluted with deionized water (1 L) and washed several times. Second, 50 mg of the obtained solid was dispersed in 30 mL concentrated $\text{NH}_3 \cdot \text{H}_2\text{O}$, and then the mixed suspension was transferred into a 20 mL Teflon-lined stainless-steel autoclave and heated at 200°C for 24 h. Upon cooling to room temperature, the precipitate was washed with water several times to remove the adsorbed NH_3 molecules. Third, 10 mg of the synthesized solid was dispersed in 100 mL of water, and then treated ultrasonically for $\sim 6 \text{ h}$. The as-obtained aqueous suspension was then centrifuged at $\sim 7000 \text{ rpm}$ and dialyzed in a dialysis bag to remove large-sized nanoparticles.

2.1.3 Preparation of $\text{g-C}_3\text{N}_4/\text{Ag}_2\text{WO}_4$ photocatalyst. The as-prepared Ag_2WO_4 nanorods (300 mg) were mixed with 200 mL of deionized water by ultrasonication for 30 min. Then, 1.0 mL of a 5% polyethylene glycol (PEG) 2000 solution was added and the dispersion was stirred for another 10 min. For wrapping $\text{g-C}_3\text{N}_4$ QDs on Ag_2WO_4 nanorods, 30 mL of the $\text{g-C}_3\text{N}_4$ QDs solution (1 mg mL^{-1}) was added and the reaction temperature was kept at 70°C for 60 min. The resulting suspension was

filtered, washed with deionized water three times, and dried at 60°C for 24 h in a vacuum oven. The theoretical wrapping amount of $\text{g-C}_3\text{N}_4$ QDs was 10 wt%.

2.1.4 Preparation of $\text{Ag}_3\text{PO}_4/\text{g-C}_3\text{N}_4/\text{Ag}_2\text{WO}_4$ photocatalyst.

The $\text{Ag}_3\text{PO}_4/\text{g-C}_3\text{N}_4/\text{Ag}_2\text{WO}_4$ hybrid photocatalyst was synthesized through an *in situ* precipitation method at room temperature. In a typical process, $\text{g-C}_3\text{N}_4/\text{Ag}_2\text{WO}_4$ nanorods (300 mg) were dispersed in 100 mL of deionized water by ultrasound for 30 min, and then an emulsion of $\text{AgNO}_3 + \text{Na}_2\text{HPO}_4$ (with a molar ratio of $\text{Ag} : \text{P} = 3 : 1$) was dropwise added to the suspension under magnetic stirring. The pH value was adjusted to 3 by adding 1.0 M NaOH. The resulting suspension was stirred in the dark for another 30 min. Finally, the precipitate was washed with deionized water three times, collected by centrifugation, and then dried at 60°C in the vacuum drying oven to obtain $\text{Ag}_3\text{PO}_4/\text{g-C}_3\text{N}_4/\text{Ag}_2\text{WO}_4$ (denoted as 10% $\text{Ag}_3\text{PO}_4/\text{g-C}_3\text{N}_4/\text{Ag}_2\text{WO}_4$, 20% $\text{Ag}_3\text{PO}_4/\text{g-C}_3\text{N}_4/\text{Ag}_2\text{WO}_4$, 30% $\text{Ag}_3\text{PO}_4/\text{g-C}_3\text{N}_4/\text{Ag}_2\text{WO}_4$, 40% $\text{Ag}_3\text{PO}_4/\text{g-C}_3\text{N}_4/\text{Ag}_2\text{WO}_4$, and 50% $\text{Ag}_3\text{PO}_4/\text{g-C}_3\text{N}_4/\text{Ag}_2\text{WO}_4$, respectively).

2.2 Characterization of photocatalysts

X-ray diffraction (XRD) was performed on a D/MAX 2500 V diffractometer (Rigaku, Japan) with monochromatized $\text{Cu K}\alpha$ radiation, $\lambda = 0.15418 \text{ nm}$, and the scanning range was from 10° to 70° . The morphologies and microstructures of the products were characterized by transmission electron microscopy (TEM, JEM-2100F). X-ray photoelectron spectroscopy (XPS, VG Scientific) using $300 \text{ W Al K}\alpha$ radiation as the excitation source was applied to study the composition and chemical state of the elements. Fourier-transform infrared spectroscopy (FT-IR) spectra were obtained with an FT-IR spectrometer (America Perkin Elmer, Spectrum One) using the standard KBr disk method. UV-vis diffuse reflection spectra (DRS) of the samples were tested on a scan UV-vis spectrophotometer (UV-2550) equipped with an integrating sphere using BaSO_4 as the reference sample. The surface areas were measured by using the nitrogen adsorption Brunauer–Emmett–Teller (BET) method (BET/BJH Surface Area, 3H-2000PS1).

2.3 Photocatalytic activities study

The photocatalytic properties of the as-prepared samples were evaluated using Rh B as a model compound. In experiments, the Rh B solution (0.01 mmol L^{-1} , 100 mL) containing 0.02 g of photocatalyst were mixed in a Pyrex reaction glass. The reactivity experiments were conducted in air at room temperature. A 300 W Xe lamp ($\lambda > 420 \text{ nm}$) with 100 mW cm^{-2} illumination intensity was employed to provide visible-light irradiation. A 420 nm cutoff filter was inserted between the lamp and the sample to filter out UV light ($\lambda < 420 \text{ nm}$). Prior to visible-light illumination, the suspension was strongly stirred in the dark for 40 min. Then the solution was exposed to visible-light irradiation under magnetic stirring. At given time intervals, 4 mL of the suspension was periodically collected and analyzed after centrifugation. The Rh B concentration was analyzed by using a UV-2550 spectrometer to record the intensity of the maximum band at 552 nm in the UV-vis absorption spectra.



2.4 Active species trapping experiments

For detecting the active species during photocatalytic reactivity, some sacrificial agents, such as 2-propanol (IPA), disodium ethylenediamine tetraacetic acid (EDTA-2Na), and 1,4-benzoquinone (BQ) were used as the hydroxyl radical ($\cdot\text{OH}$) scavenger, hole (h^+) scavenger, and superoxide radical ($\text{O}_2^{\cdot-}$) scavenger, respectively. The method was similar to the former photocatalytic activity test with the addition of 1 mmol of quencher in the presence of Rh B.

3. Results and discussion

To determine the crystal form of as-prepared samples, the XRD patterns were recorded, as shown in Fig. 1. Pure Ag_2WO_4 shows obvious diffraction peaks at $2\theta = 30.2^\circ$, 31.4° , 33.0° , and 45.4° , which are attributed to the (002), (231), (400), and (402) diffraction planes of $\alpha\text{-Ag}_2\text{WO}_4$ (JCPDS no. 34-0061), respectively.²⁵ For the pure $\text{g-C}_3\text{N}_4$ sample, the diffraction peak at 27.4° can be clearly observed, which are indexed to (002) plane of $\text{g-C}_3\text{N}_4$.²⁶ From the XRD pattern of the $\text{g-C}_3\text{N}_4/\text{Ag}_2\text{WO}_4$ composite, all the crystal planes of $\alpha\text{-Ag}_2\text{WO}_4$ can be detected. However, there are no any diffraction peaks of $\text{g-C}_3\text{N}_4$ that can be observed for the $\text{g-C}_3\text{N}_4/\text{Ag}_2\text{WO}_4$ sample, owing to small crystal size of $\text{g-C}_3\text{N}_4$ QDs.²⁶ For the pure Ag_3PO_4 , the diffraction peaks can be indexed to the cubic structure of Ag_3PO_4 (JCPDS 06-0505). The diffraction peaks of Ag_3PO_4 are clearly observed in $\text{Ag}_3\text{PO}_4/\text{g-C}_3\text{N}_4/\text{Ag}_2\text{WO}_4$ composites, and the intensities of the diffraction peaks of Ag_3PO_4 increase with increasing weight ratio of Ag_3PO_4 in the composites.

Herein, the successful loading of $\text{g-C}_3\text{N}_4$ QDs was illustrated by FT-IR spectra, as displayed in Fig. 2. The main characteristic peaks of $\text{g-C}_3\text{N}_4$ QDs are observed in both $\text{g-C}_3\text{N}_4/\text{Ag}_2\text{WO}_4$ and $\text{Ag}_3\text{PO}_4/\text{g-C}_3\text{N}_4/\text{Ag}_2\text{WO}_4$ spectra, showing the successful loading of $\text{g-C}_3\text{N}_4$ QDs. The absorption bands at $1700\text{--}800\text{ cm}^{-1}$ are attributed to either $\text{C}=\text{N}$ or C-N stretching vibrations.¹⁹ The broad range centered at 3200 cm^{-1} can be ascribed to the N-H stretching vibration.¹⁹

XPS measurement was also employed to investigate the surface chemical states of the $\text{Ag}_3\text{PO}_4/\text{g-C}_3\text{N}_4/\text{Ag}_2\text{WO}_4$ composite. Fig. 3a shows the XPS spectrum of Ag 3d; two

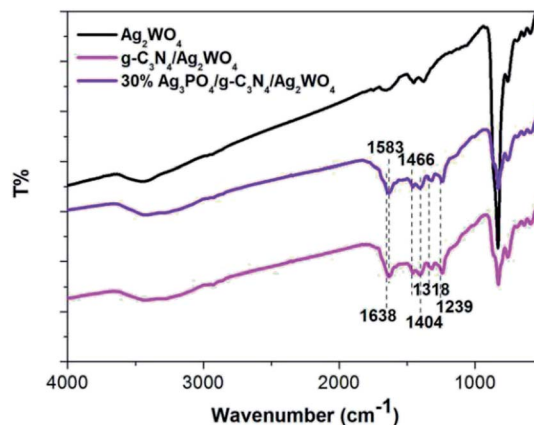


Fig. 2 FT-IR spectra of the as-prepared samples.

different peaks centered at binding energies of 366.5 and 372.6 eV can be detected, and these are assigned to $\text{Ag } 3\text{d}_{5/2}$ and $\text{Ag } 3\text{d}_{3/2}$,²⁷ respectively. The XPS spectrum of W 4f shows two different peaks centered at 38.3 and 36.1 eV , which are ascribed to $\text{W } 4\text{f}_{5/2}$ and $\text{W } 4\text{f}_{7/2}$, respectively (Fig. 3b).²⁶ The P 2p peak is observed at $\sim 134.1\text{ eV}$ (Fig. 3c), corresponding to P^{5+} .²⁷ As can be seen in the XPS spectrum of C 1s (Fig. 3d), the peak at 283.3 eV can be assigned to the sp^2 -bonded carbon in C-C, whereas the peak located at 287.0 eV reveals the formation of $\text{N-C}=\text{N}$.¹⁹ The XPS spectrum of N 1s can be deconvoluted into two peaks with binding energies at 397.5 and 400.0 eV , which are attributed to $\text{C-N}=\text{C}$ and $(\text{N-C})_3$,¹⁹ respectively.

Fig. 4 shows scanning electron microscopy (SEM) images of pure Ag_2WO_4 and the $\text{Ag}_3\text{PO}_4/\text{g-C}_3\text{N}_4/\text{Ag}_2\text{WO}_4$ composite. Fig. 4a shows a rod-like structure, and the average diameter of the nanorods was $\sim 100\text{ nm}$. The $\text{Ag}_3\text{PO}_4/\text{g-C}_3\text{N}_4/\text{Ag}_2\text{WO}_4$ composite displays a similar morphology to that of pure Ag_2WO_4 (Fig. 4b), showing that loading Ag_3PO_4 nanocrystals and $\text{g-C}_3\text{N}_4$ QDs did not have any significant influence on the morphology of the Ag_2WO_4 nanorods. The as-prepared Ag_3PO_4 sample was composed of nanocrystals with average sizes of $\sim 20\text{ nm}$ (Fig. S1†). A TEM image of $\text{g-C}_3\text{N}_4$ QDs is shown in Fig. S2†, revealing that the prepared $\text{g-C}_3\text{N}_4$ QDs are mono-dispersed in the water solution and that each QD is uniform in size. Fig. 4c shows a TEM image of an individual $\text{Ag}_3\text{PO}_4/\text{g-C}_3\text{N}_4/\text{Ag}_2\text{WO}_4$ nanorod. It can be seen that Ag_3PO_4 nanocrystals and $\text{g-C}_3\text{N}_4$ QDs were loaded on the surface of the Ag_2WO_4 nanorod. A high-resolution TEM image of the $\text{Ag}_3\text{PO}_4/\text{g-C}_3\text{N}_4/\text{Ag}_2\text{WO}_4$ composite reveals that the crystal lattice fringe patterns are ~ 0.336 and $\sim 0.213\text{ nm}$ (Fig. 4d), which correspond to the (002) crystal plane of $\text{g-C}_3\text{N}_4$ and the (210) crystal plane of Ag_3PO_4 , respectively. The lattice distance of 0.229 nm in the nanorod is correlated to the (421) crystal plane of Ag_2WO_4 (Fig. 4e).

The BET surface areas of pure Ag_2WO_4 and $\text{Ag}_3\text{PO}_4/\text{g-C}_3\text{N}_4/\text{Ag}_2\text{WO}_4$ were analyzed using an automated surface area analyzer (Fig. 5). The calculated BET surface area of $\text{Ag}_3\text{PO}_4/\text{g-C}_3\text{N}_4/\text{Ag}_2\text{WO}_4$ is $110.602\text{ m}^2\text{ g}^{-1}$, which is larger than that of pure Ag_2WO_4 ($20.817\text{ m}^2\text{ g}^{-1}$). It can be concluded that the loading of Ag_3PO_4 and $\text{g-C}_3\text{N}_4$ QDs can facilitate more efficient

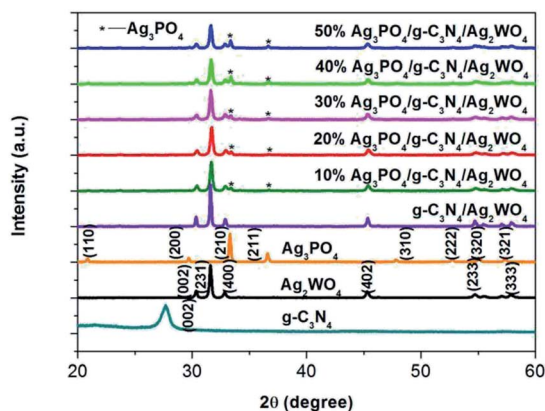


Fig. 1 XRD patterns of the as-prepared samples.



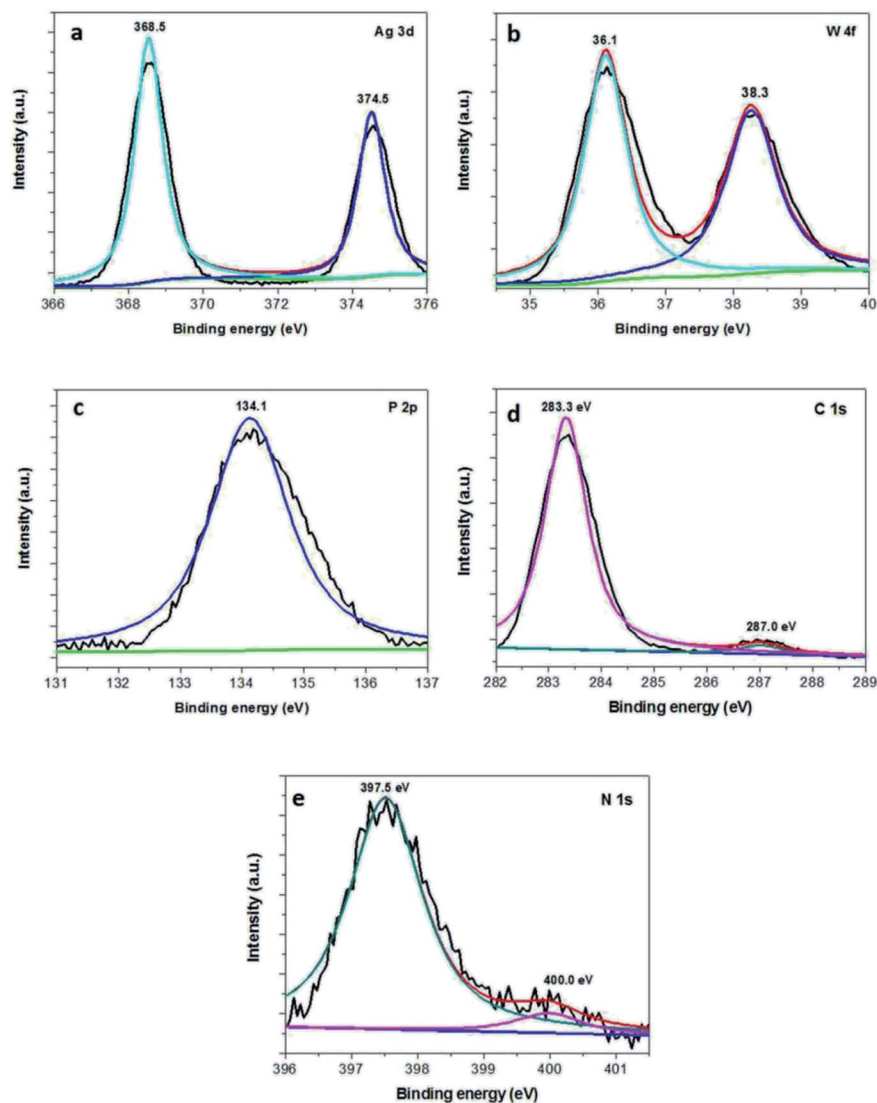


Fig. 3 XPS spectra of the as-obtained 30% $\text{Ag}_3\text{PO}_4/\text{g-C}_3\text{N}_4/\text{Ag}_2\text{WO}_4$: (a) Ag 3d, (b) W 4f, (c) P 2p, (d) C 1s, and (e) N 1s.

contact of the $\text{Ag}_3\text{PO}_4/\text{g-C}_3\text{N}_4/\text{Ag}_2\text{WO}_4$ composite with organic contaminants, which is beneficial to the improvement of photocatalytic performance.¹⁹

UV-vis DRS are shown in Fig. 6 to study the optical absorption properties of the $\text{Ag}_3\text{PO}_4/\text{g-C}_3\text{N}_4/\text{Ag}_2\text{WO}_4$ composite. The band gap of anatase Ag_2WO_4 is ~ 3.20 eV, so its absorption onset is located at 410 nm. The band gap for $\text{g-C}_3\text{N}_4$ QDs is 2.75 eV, corresponding to the absorption onset of 450 nm. In addition, the band gap of Ag_3PO_4 is calculated to be 2.13 eV, indicating an absorption onset at ~ 580 nm. In comparison with pure Ag_2WO_4 , the $\text{Ag}_3\text{PO}_4/\text{g-C}_3\text{N}_4/\text{Ag}_2\text{WO}_4$ composite shows an absorption in the visible range that accompanies a red shift in the absorption edge resulting from the synergistic effect among Ag_2WO_4 , Ag_3PO_4 , and $\text{g-C}_3\text{N}_4$. The results reveal that the obtained $\text{Ag}_3\text{PO}_4/\text{g-C}_3\text{N}_4/\text{Ag}_2\text{WO}_4$ composite could be employed as a visible-light photocatalyst. The chronoamperometric $I-t$ curves are shown in Fig. S3.† Compared with pure Ag_2WO_4 , the $\text{Ag}_3\text{PO}_4/\text{g-C}_3\text{N}_4/\text{Ag}_2\text{WO}_4$ composite exhibited enhanced

photocurrent responses. The ternary nanoheterojunctions can facilitate photoelectron-hole separation and thus retard photoelectron-hole recombination in the $\text{Ag}_3\text{PO}_4/\text{g-C}_3\text{N}_4/\text{Ag}_2\text{WO}_4$ composite.^{28–30}

In this study, $\text{Ag}_3\text{PO}_4/\text{g-C}_3\text{N}_4/\text{Ag}_2\text{WO}_4$ along with sole Ag_2WO_4 and $\text{g-C}_3\text{N}_4/\text{Ag}_2\text{WO}_4$ composite was tested for photocatalytic Rh B degradation under visible-light irradiation (Fig. 7a). The blank experiment demonstrated that Rh B was stable under visible-light irradiation for 80 min. The pure Ag_2WO_4 composite exhibited generally low photocatalytic performances, with only 40.0% Rh B degradation, after 80 min visible-light irradiation. The low performance is probably due to the fast recombination of photoinduced charges in the single Ag_2WO_4 . Compared with the pure Ag_2WO_4 sample, the $\text{g-C}_3\text{N}_4/\text{Ag}_2\text{WO}_4$ composite exhibited enhanced photocatalytic efficiency (50% Rh B degradation). The photocatalytic activity of $\text{Ag}_3\text{PO}_4/\text{g-C}_3\text{N}_4/\text{Ag}_2\text{WO}_4$ further improved the degradation of Rh B under visible light ($\lambda > 420$ nm), which can be ascribed to the



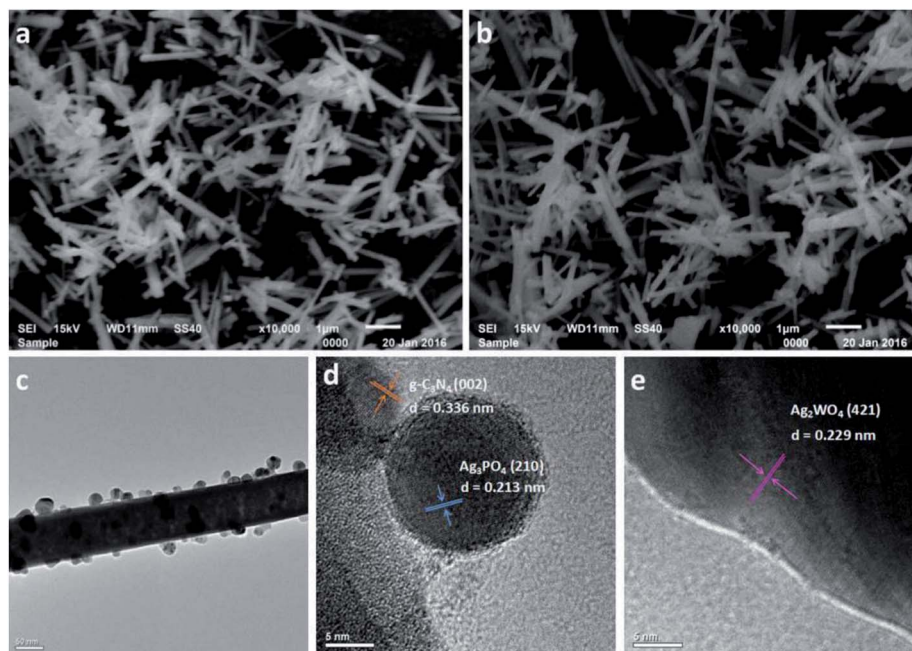


Fig. 4 SEM images of the as-prepared samples: (a) Ag_2WO_4 and (b) 30% $\text{Ag}_3\text{PO}_4/\text{g-C}_3\text{N}_4/\text{Ag}_2\text{WO}_4$. (c) TEM image of 30% $\text{Ag}_3\text{PO}_4/\text{g-C}_3\text{N}_4/\text{Ag}_2\text{WO}_4$. (d and e) High-resolution TEM images of 30% $\text{Ag}_3\text{PO}_4/\text{g-C}_3\text{N}_4/\text{Ag}_2\text{WO}_4$.

efficient separation of photogenerated electrons and holes through the ternary heterostructure. Among the $\text{Ag}_3\text{PO}_4/\text{g-C}_3\text{N}_4/\text{Ag}_2\text{WO}_4$ nanocomposites, the highest activity was obtained with the 30% Ag_3PO_4 loading sample, with which almost 100% of Rh B was photodegraded after 80 min of visible-light irradiation. This is because hybridization of Ag_2WO_4 with Ag_3PO_4 can result in efficient separation of photogenerated charges, thus improving the photocatalytic performance. However, too many Ag_3PO_4 can even cover the surface of Ag_2WO_4 , which can reduce the density of active sites, thus reducing the photocatalytic efficiency. Therefore, the suitable loading content of Ag_3PO_4 is a primary prerequisite for optimizing the photocatalytic reaction.

It is important to study the active species in the photocatalysis process. As shown in Fig. 7b, the photocatalytic efficiency of the 30% $\text{Ag}_3\text{PO}_4/\text{g-C}_3\text{N}_4/\text{Ag}_2\text{WO}_4$ composite was greatly suppressed after the addition of BQ and EDTA-2Na, indicating that $\text{O}_2^{\cdot-}$ and h^+ were the main reactive species. In addition, a slight decrease in the photocatalytic activity was observed by the addition of IPA, suggesting that $\cdot\text{OH}$ was not the main reactive species.

The stability of the 30% $\text{Ag}_3\text{PO}_4/\text{g-C}_3\text{N}_4/\text{Ag}_2\text{WO}_4$ photocatalyst was studied through performing recycle experiments, as shown in Fig. 8. After four photocatalytic runs, the photocatalytic efficiency did not display any significant decay. The stability of the photocatalyst was also studied by using XRD (Fig. 9a) and SEM analysis (Fig. 9b) of fresh and used 30% $\text{Ag}_3\text{PO}_4/\text{g-C}_3\text{N}_4/\text{Ag}_2\text{WO}_4$. It can be seen that the phase structure, as well as the morphology of the 30% $\text{Ag}_3\text{PO}_4/\text{g-C}_3\text{N}_4/\text{Ag}_2\text{WO}_4$, remains intact after four recycles, revealing the high stability of the 30% $\text{Ag}_3\text{PO}_4/\text{g-C}_3\text{N}_4/\text{Ag}_2\text{WO}_4$ photocatalyst.

Based on the results and discussion above, heterostructure formed in the $\text{g-C}_3\text{N}_4/\text{Ag}/\text{BiVO}_4$ photocatalyst played an important role in the efficient separation of photoinduced charges. The potentials of VB and CB of a semiconductor can be calculated according to the following empirical equations:

$$E_{\text{VB}} = X - E^{\text{e}} + 0.5E_{\text{g}} \quad (1)$$

$$E_{\text{CB}} = E_{\text{VB}} - E_{\text{g}} \quad (2)$$

where E_{VB} is the valence band edge potential, E_{CB} is the conduction band edge potential, X is the electronegativity of the semiconductor, which is the geometric mean of the electronegativity of the constituent atoms, E^{e} is the energy of free

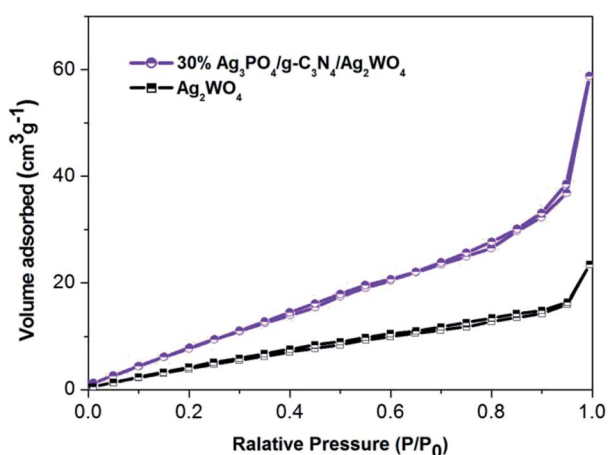


Fig. 5 N_2 adsorption-desorption isotherm curves of the as-prepared samples.



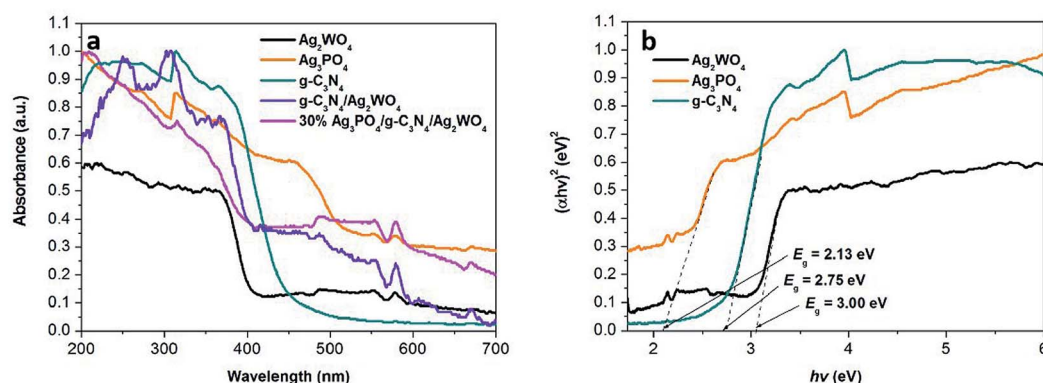


Fig. 6 UV-vis diffuse reflection spectra of the as-obtained samples. (b) Plots of $(\alpha h\nu)^2$ versus photon energy ($h\nu$) for the band gap energies of Ag_3PO_4 , $\text{g-C}_3\text{N}_4$, and Ag_2WO_4 .

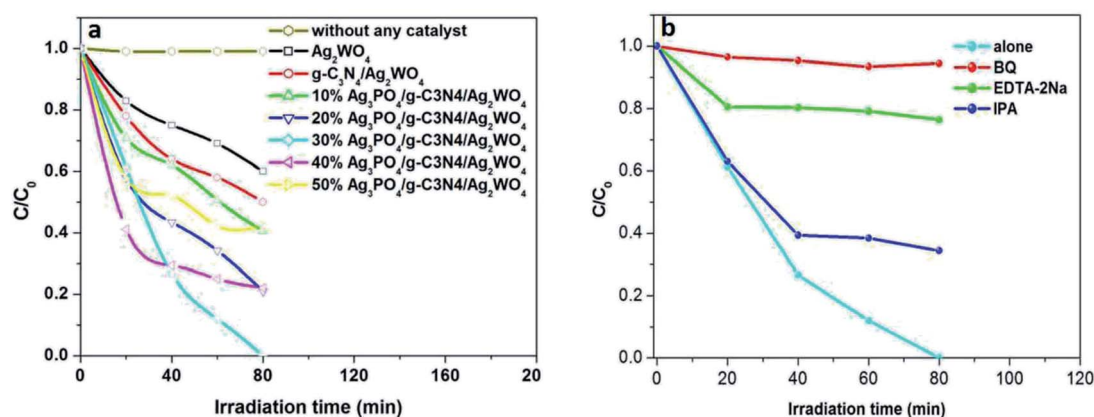


Fig. 7 (a) Photodegradation efficiencies of Rh B as a function of irradiation time for different photocatalysts. (b) Trapping experiment of active species during the photocatalytic degradation of Rh B over $\text{C}_{60}\text{CNTs/bismuth-based oxide nanocomposites}$ under visible-light irradiation.

electrons on the hydrogen scale (about 4.5 eV), E_g is the band gap energy of the semiconductor. According to the DRS characterization results (Fig. 6) and eqn (1) and (2), the valence band

(VB) edges of $\text{g-C}_3\text{N}_4$ QDs, Ag_2WO_4 , and Ag_3PO_4 were measured to be +1.585, 2.73, and 2.535 eV *versus* SHE, respectively, while the conduction band (CB) edges for $\text{g-C}_3\text{N}_4$ QDs, Ag_2WO_4 , and Ag_3PO_4 were -1.165 , -0.27 , and 0.505 eV *versus* SHE, respectively.

Fig. 10 shows the proposed mechanism for the charge-carrier transfer process in the $\text{Ag}_3\text{PO}_4/\text{g-C}_3\text{N}_4/\text{Ag}_2\text{WO}_4$ photocatalyst. When the $\text{Ag}_3\text{PO}_4/\text{g-C}_3\text{N}_4/\text{Ag}_2\text{WO}_4$ composite is irradiated, electrons can be excited from CBs of $\text{g-C}_3\text{N}_4$ QDs and Ag_3PO_4 . Because the CB position of $\text{g-C}_3\text{N}_4$ QDs was more negative than that of Ag_2WO_4 and Ag_3PO_4 , the photo-generated electrons in the CB of $\text{g-C}_3\text{N}_4$ QDs can easily flow into the CB of Ag_2WO_4 or Ag_3PO_4 , leading to the redistribution of electrons and holes so that the oxidation reaction is highly likely to take place and effectively prevent the electron-hole recombination process. Resulting in the improved photocatalytic performance of the $\text{Ag}_3\text{PO}_4/\text{g-C}_3\text{N}_4/\text{Ag}_2\text{WO}_4$ composite photocatalyst. The holes in the VB of Ag_3PO_4 with strong oxidation power can directly degrade Rh B. In addition, the electrons on the $\text{g-C}_3\text{N}_4$ can react with O_2 to produce $\cdot\text{O}_2^-$, which can completely oxidize organic molecules to water and carbon dioxide.^{31,32}

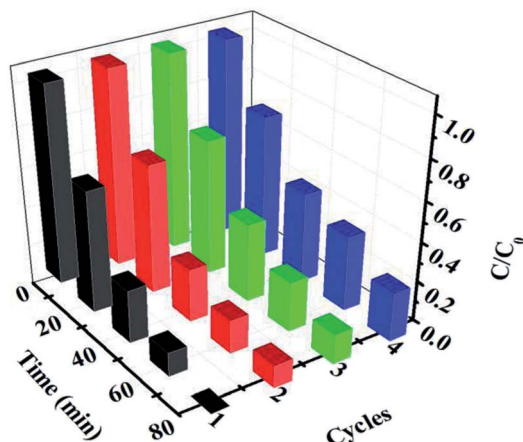


Fig. 8 Cycling runs for the photocatalytic degradation of Rh B over the ternary nanocomposites under visible-light irradiation.



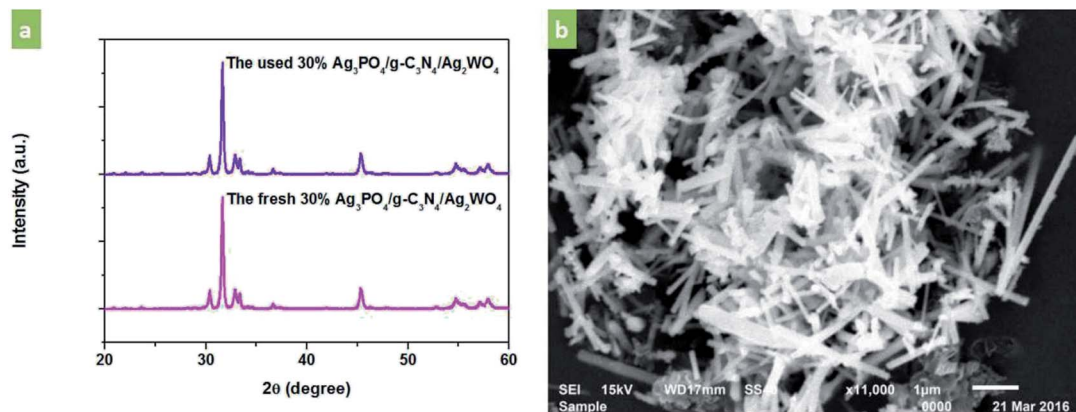


Fig. 9 (a) XRD patterns of the as-prepared 30% $\text{Ag}_3\text{PO}_4/\text{g-C}_3\text{N}_4/\text{Ag}_2\text{WO}_4$ sample before and after photocatalysis. (b) SEM image of the 30% $\text{Ag}_3\text{PO}_4/\text{g-C}_3\text{N}_4/\text{Ag}_2\text{WO}_4$ sample after photocatalysis.

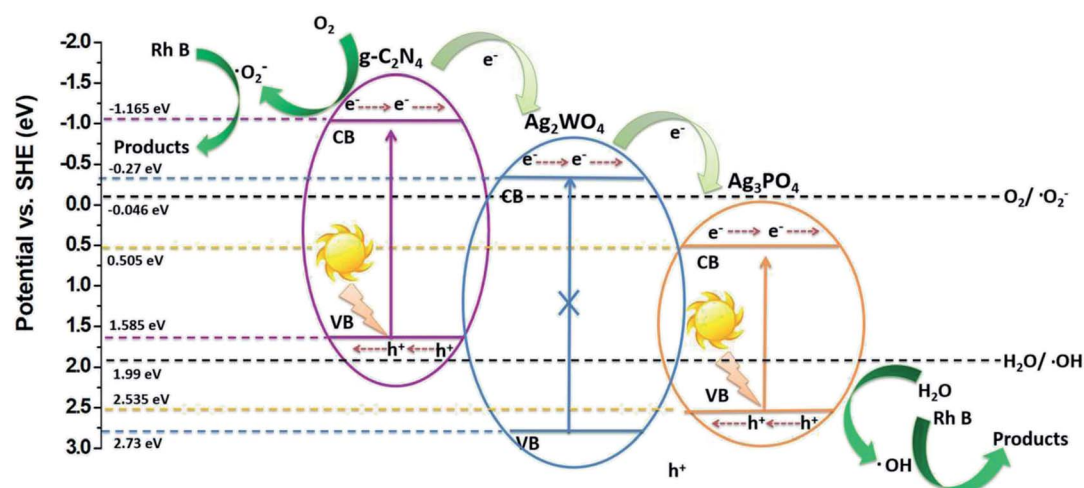


Fig. 10 Schematic diagram of the separation and transfer of photogenerated charges in the $\text{Ag}_3\text{PO}_4/\text{g-C}_3\text{N}_4/\text{Ag}_2\text{WO}_4$ composite photocatalyst under visible-light irradiation.

4. Conclusions

In summary, novel $\text{Ag}_3\text{PO}_4/\text{g-C}_3\text{N}_4/\text{Ag}_2\text{WO}_4$ nanorods were successfully synthesized by using simple deposition-precipitation of Ag_3PO_4 nanocrystals and $\text{g-C}_3\text{N}_4$ QDs on Ag_2WO_4 nanorods. The as-prepared $\text{Ag}_3\text{PO}_4/\text{g-C}_3\text{N}_4/\text{Ag}_2\text{WO}_4$ nanostructures showed excellent photocatalytic performance on the decolorization of Rh B, which was superior to those of pure Ag_2WO_4 , or $\text{g-C}_3\text{N}_4/\text{Ag}_2\text{WO}_4$ under visible-light irradiation ($\lambda > 420$ nm). The Ag_3PO_4 and $\text{g-C}_3\text{N}_4$ loading contributed to enhanced visible-light harvesting and reduced recombination of photo-generated electron-hole pairs owing to the synergistic effect of the heterojunction structure of $\text{Ag}_3\text{PO}_4/\text{g-C}_3\text{N}_4/\text{Ag}_2\text{WO}_4$, thereby leading to enhanced photocatalytic performance.

Conflicts of interest

There are no conflicts to declare.

Acknowledgements

This work was supported by the National Natural Science Foundation of China (21407059, 51603086) and the Open Subject of the State Key Laboratory of Rare Earth Resource Utilization (RERU2017011).

References

- 1 D. Wang, Y. Duan, Q. Luo, X. Li and L. Bao, *Desalination*, 2011, **270**, 174–180.
- 2 H. G. Yu, L. Liu, X. F. Wang, P. Wang, J. G. Yu and Y. H. Wang, *Dalton Trans.*, 2012, **41**, 10405–10411.
- 3 H. J. Dong, G. Chen, J. X. Sun, C. M. Li, Y. G. Yu and D. H. Chen, *Appl. Catal., B*, 2013, **134**, 46–54.
- 4 C. Dong, K. L. Wu, X. W. Wei, X. Z. Li, L. Liu, T. H. Ding, J. Wang and Y. Ye, *CrystEngComm*, 2014, **16**, 730–736.



- 5 X. F. Wang, S. F. Li, H. G. Yu, J. G. Yu and S. W. Liu, *Chem. – Eur. J.*, 2011, **17**, 7777–7780.
- 6 Y. P. Bi, S. X. Ouyang, N. Umezawa, J. Y. Cao and J. H. Ye, *J. Am. Chem. Soc.*, 2011, **133**, 6490–6492.
- 7 H. P. Chen, N. Chen, C. P. Feng and Y. Gao, *J. Colloid Interface Sci.*, 2018, **515**, 119–128.
- 8 D. F. Xu, B. Cheng, S. W. Cao and J. G. Yu, *Appl. Catal., B*, 2015, **164**, 380–388.
- 9 S. Mandal and R. Ananthakrishnan, *ACS Sustainable Chem. Eng.*, 2018, **6**(1), 1091–1104.
- 10 Z. Y. Lin, J. L. Li, Z. Q. Zheng, J. H. Yan, P. Liu, C. X. Wang and G. W. Yang, *ACS Nano*, 2015, **9**, 7256–7265.
- 11 X. F. Wang, S. Zhan, Y. Wang, P. Wang, H. G. Yu, J. G. Yu and C. Z. Hu, *J. Colloid Interface Sci.*, 2014, **422**, 30–37.
- 12 X. H. Liu, J. L. Hu, J. J. Li, Y. Hu, Y. Shao, H. J. Yang, G. X. Tong and H. S. Qian, *Mater. Lett.*, 2013, **91**, 129–132.
- 13 V. M. Longo, C. C. D. Foggi, M. M. Ferrer, A. F. Gouveia, R. S. André, W. Avansi, C. E. Vergani, A. L. Machado, J. André, L. S. Cavalcante, A. C. Hernandez and E. Longo, *J. Phys. Chem. A*, 2014, **118**, 5769–5778.
- 14 L. Liu, Y. H. Qi, J. R. Lu, S. L. Lin, W. J. An, Y. H. Liang and W. Q. Cui, *Appl. Catal., B*, 2016, **183**, 133–141.
- 15 E. Grilla, A. Petala, Z. Frontistis, I. K. Konstantinou, D. I. Kondarides and D. Mantzavinos, *Appl. Catal., B*, 2018, **231**, 73–81.
- 16 L. Liu, L. Ding, Y. G. Liu, W. J. An, S. L. Lin, Y. H. Liang and W. Q. Cui, *Appl. Catal., B*, 2017, **201**, 92–104.
- 17 W. B. Li, C. Feng, S. Y. Dai, J. G. Yue, F. X. Hua and H. Hou, *Appl. Catal., B*, 2015, **168**, 465–471.
- 18 W. J. Shan, Y. Hu, Z. G. Bai, M. M. Zheng and C. H. Wei, *Appl. Catal., B*, 2016, **188**, 1–12.
- 19 J. Y. Su, L. Zhu and G. H. Chen, *Appl. Catal., B*, 2016, **186**, 127–135.
- 20 L. Xu, H. N. Li, J. X. Xia, L. G. Wang, H. Xu, H. Y. Ji, H. M. Li and K. Y. Sun, *Mater. Lett.*, 2014, **128**, 349–353.
- 21 Y. Wang, G. Q. Tan, T. Liu, Y. N. Su, H. J. Ren, X. L. Zhang, A. Xia, L. Lv and Y. Liu, *Appl. Catal., B*, 2018, **234**, 37–49.
- 22 X. L. Liu, P. Wang, H. S. Zhai, Q. Q. Zhang, B. B. Huang, Z. Y. Wang, Y. Y. Liu, Y. Dai, X. Y. Qin and X. Y. Zhang, *Appl. Catal., B*, 2018, **232**, 521–530.
- 23 D. F. Xu, B. Cheng, W. K. Wang, C. J. Jiang and J. G. Yu, *Appl. Catal., B*, 2018, **231**, 368–380.
- 24 W. J. Wang, J. C. Yu, Z. R. Shen, D. K. L. Chan and T. Gu, *Chem. Commun.*, 2014, **50**, 10148–10150.
- 25 Z. Y. Lin, J. L. Li, Z. Q. Zheng, J. H. Yan, P. Liu, C. X. Wang and G. W. Yang, *ACS Nano*, 2015, **9**, 7256–7265.
- 26 X. P. Wang, L. X. Wang, F. Zhao, C. G. Hu, Y. Zhao, Z. P. Zhang, S. L. Chen, G. Q. Shi and L. T. Qu, *Nanoscale*, 2015, **7**, 3035–3042.
- 27 L. Liu, Y. H. Qi, J. R. Lu, S. L. Lin, W. J. An, Y. H. Liang and W. Q. Cui, *Appl. Catal., B*, 2016, **183**, 133–141.
- 28 S. H. Zhan, Q. L. Hou, Y. Li, S. L. Ma, P. F. Wang, Y. N. Li and H. T. Wang, *RSC Adv.*, 2018, **8**, 34428–34436.
- 29 C. Wang, G. L. Wang, X. F. Zhang, X. L. Dong, C. Ma, X. X. Zhang, H. C. Ma and M. Xue, *RSC Adv.*, 2018, **8**, 18419–18426.
- 30 Y. J. Zou, J. W. Shi, D. D. Ma, Z. Y. Fan, C. M. Niu and L. Z. Wang, *Chemcatchem*, 2017, **9**, 3752–3761.
- 31 B. C. Zhu, P. F. Xia, Y. Li, W. K. Ho and J. G. Yu, *Appl. Surf. Sci.*, 2017, **391**, 175–183.
- 32 W. Liu, J. Shen, X. F. Yang, Q. Q. Liu and H. Tang, *Appl. Surf. Sci.*, 2018, **456**, 369–378.

